Journal of Zhejiang University SCIENCE A
ISSN 1009-3095 (Print); ISSN 1862-1775 (Online)
www.zju.edu.cn/jzus; www.springerlink.com
E-mail: jzus@zju.edu.cn

Optimization study of a PEM fuel cell performance using 3D multi-phase computational fluid dynamics model*

AL-BAGHDADI Maher A.R. Sadiq†, AL-JANABI Haroun A.K. Shahad
(*Department of Mechanical Engineering, International Technological University, London NW2 6HS, UK*)
†E-mail: maherars@hotmail.com

Received Aug. 31, 2006; revision accepted Oct. 24, 2006

Abstract: An optimization study using a comprehensive 3D, multi-phase, non-isothermal model of a PEM (proton exchange membrane) fuel cell that incorporates significant physical processes and key parameters affecting fuel cell performance is presented and discussed in detail. The model accounts for both gas and liquid phase in the same computational domain, and thus allows for the implementation of phase change inside the gas diffusion layers. The model includes the transport of gaseous species, liquid water, protons, energy, and water dissolved in the ion-conducting polymer. Water is assumed to be exchanged among three phases: liquid, vapour, and dissolved, with equilibrium among these phases being assumed. This model also takes into account convection and diffusion of different species in the channels as well as in the porous gas diffusion layer, heat transfer in the solids as well as in the gases, and electrochemical reactions. The results showed that the present multi-phase model is capable of identifying important parameters for the wetting behaviour of the gas diffusion layers and can be used to identify conditions that might lead to the onset of pore plugging, which has a detrimental effect on the fuel cell performance. This model is used to study the effects of several operating, design, and material parameters on fuel cell performance. Detailed analyses of the fuel cell performance under various operating conditions have been conducted and examined.

Key words: Optimization, PEM fuel cell, Multi-phase, Water transport, CFD (computational fluid dynamics)
doi:10.1631/jzus.2007.A0285 **Document code:** A **CLC number:** TP273

INTRODUCTION

Water management is one of the critical operation issues in proton exchange membrane (PEM) fuel cells. Spatially varying concentrations of water in both vapour and liquid form are expected throughout the cell because of varying rates of production and transport (Sui and Djilali, 2005). Devising better water management is therefore a key issue in PEMFC design, and this requires improved understanding of the parameters affecting water transport in the membrane. Proper thermal management is also required to remove the heat produced by the electrochemical reaction in order to prevent drying out of the membrane, which in turn can result not only in reduced performance but also in eventual rupture of the membrane (Ju *et al*., 2005). The small temperature differentials between the fuel cell stack and the operating environment make thermal management a challenging problem in PEM fuel cells. Thermal management is also essential for the control of the water evaporation or condensation rates. As a result of the changes in temperature, the PEM, GDL (gas diffusion layer) and bipolar plates will all experience expansion and contraction. Because of the different thermal expansion coefficients between these materials, thermal stresses are introduced into the unit cell during operation. In addition, the non-uniform current and reactant flow distributions in the cell can result in non-uniform temperature of the cell (temperature gradient), which could in turn, potentially cause localized increases in the stress magnitudes (Tang *et al*., 2006). The durability of PEMs used in fuel cells is a

* Project supported by the Postgraduate Programs of the International Technological University (ITU), London, UK

major factor in the operating lifetime of fuel cell systems. Durability is a complicated phenomenon linked to the chemical and mechanical interactions of the fuel cell components, i.e., electro-catalysts, membranes, gas diffusion layers, and bipolar plates, under severe environmental conditions, such as elevated temperature (Tang *et al*., 2006). Mechanical damage in the PEM can appear as through-the-thickness flaws or pinholes in the membrane, or delaminating between the polymer membrane and gas diffusion layers. The results are in gradual reduction of ionic conductivity, increase in the total cell resistance, and reduction of voltage and loss of output power (Stanic and Hoberecht, 2004).

The difficult experimental environment of fuel cell systems has stimulated efforts to develop models that could simulate and predict multi-dimensional coupled transport of reactants, heat and charged species using computational fluid dynamics (CFD) methods. A comprehensive computational model should include the equations and other numerical relations needed to fully define fuel cell behaviour over the range of interest. Early multi-dimensional models described gas transport in the flow channels, gas diffusion layers, and the membrane (Berning *et al*., 2002; Berning and Djilali, 2003a; Um and Wang, 2004). Recently, there has been an interest in describing operating regimes dominated by mass transport limitations resulting, in part, from the formation and transport of liquid water within the fuel cell. To model fuel cell performance in these regimes, it is necessary to include equations that describe not only the motion of water within the liquid phase, but also mass transfer between phases.

Siegel *et al*.(2004) developed a multi-phase, 2D model to account for liquid water saturation and flooding effect, and they have been studied in transport limitations due to water build up in the cathode catalyst region. In a real PEM fuel cell geometry, the gas diffusion layers are used to enhance the reaction area accessible by the reactants. The effect of using these diffusion layers is to allow a spatial distribution in the current density on the membrane in both the direction of bulk flow and the direction orthogonal to the flow but parallel to the membrane. This 2D distribution cannot be modelled with the well-used 2D models where the mass-transport limitation is absent in the third direction.

Berning and Djilali (2003b) developed a CFD multiphase model of a PEM fuel cell. Their model accounts for 3D transport processes including phase change and heat transfer, and including the gas diffusion layers and gas flow channels for both anode and cathode, as well as a cooling channel. The physics of phase change was accounted for by prescribing local evaporation as a function of the undersaturation and liquid water concentration. This model provides information on liquid water saturation and flooding under various conditions, but does not account for water dissolved in the ion-conducting polymer to calculate water content through the membrane.

Hu *et al*.(2004a; 2004b) developed an isothermal, 3D, two-phase model for a PEM fuel cell. Their model accounts for the transport of liquid water within the porous electrodes and water dissolved in the ion-conducting polymer. In addition to being restricted to constant cell temperature, the simulations presented so far using the mixture model are restricted to low humidity inlet feed streams.

Coppo *et al*.(2005) developed a multi-phase, 3D model to account for the temperature dependence of all of the physical properties involved in the model formulation and to describe liquid water removal from the GDL surface by advection due to the interaction of the water droplets and the gas stream in the gas flow channels. Their results showed that both liquid water transport within the GDL and liquid water removal from the surface of the GDL play crucial roles in determining variations in cell performance with temperature.

Simulations of 3D-PEM fuel cell geometries have required some simplifications in order to reduce computational requirements. In particular, it is only very recently that those CFD-based models have started to account for non-uniform distributions of overpotentials at the electrodes (Nguyen *et al*., 2004; Sivertsen and Djilali, 2005). These models provide comprehensive details on the distribution of reactants and allow sensitivity analysis and prediction of performance under various conditions, but they do not account for phase change, liquid water concentration in the electrodes, and water dissolved in the ion-conducting polymer. A common issue to many computational models is the uncertainties associated with the specification of various parameters that impact the transport processes. Assessing the sensitivity

of the flow, thermal or electrochemical response to these uncertainties is essential.

The development of physically representative models that allow reliable simulation of the processes under realistic conditions is essential to the development and optimization of fuel cells, the introduction of cheaper materials and fabrication techniques, and the design and development of novel architectures. Recently, Wang *et al*.(2003) and Berning and Djilali (2003a) conducted a parametric study using a single-phase 3D model. The impact of liquid water on transport in the gas-diffusion electrode was, however, not accounted for. Liquid water impacts are inherently parametric study, but no studies have yet been published to address this.

MODEL DESCRIPTION

The present work presents a comprehensive 3D, multi-phase, non-isothermal model of a PEM fuel cell that incorporates the significant physical processes and the key parameters affecting fuel cell performance. The model accounts for both gas and liquid phase in the same computational domain, and thus allows for the implementation of phase change inside the gas diffusion layers. Phase change occurs only within the porous electrodes, i.e. phase change of water inside the channels or at the channel/wall interfaces is not accounted for. The gas composition of the cathode inlet stream consists of three gas species, oxygen, nitrogen, and water vapour, while the composition of the anode inlet stream is much simpler since there are only two gas species, hydrogen and water vapour. The catalyst layer is assumed to be a thin interface where sink and source terms for the reactants and enthalpy are specified. The model includes the transport of gaseous species, liquid water, protons, energy, and water dissolved in the ion-conducting polymer. Water transport inside the porous gas diffusion layer and catalyst layer is described by two physical mechanisms: viscous drag and capillary pressure forces, and is described by advection within the gas channels. Water transport across the membrane is also described by two physical mechanisms: electro-osmotic drag and diffusion. Water is assumed to be exchanged among three phases: liquid, vapour, and dissolved, and equilibrium among these phases is assumed. The model features an algorithm that allows for a more realistic representation of the local activation overpotentials, which leads to improved prediction of the local current density distribution. This model also takes into account convection and diffusion of different species in the channels as well as in the porous gas diffusion layer, heat transfer in the solids as well as in the gases, and electrochemical reactions.

The model reflects the influence of numerous parameters on fuel cell performance including geometry, materials, operating conditions, etc. This paper describes the development of the model, the determination of properties for use in the model, the validation of the model using experimental data, and the application of the model to explain observed experimental phenomena. Optimization study using this model has been performed. The study quantifies the impact of operating conditions, design, and material parameters on fuel cell performance.

Computational domain

A computational model of an entire cell would require very large computing resources and excessively long simulation times. The computational domain in this study is therefore limited to one straight flow channel with the land areas. The full computational domain consists of cathode and anode gas flow channels, and the membrane electrode assembly as shown in Fig.1.

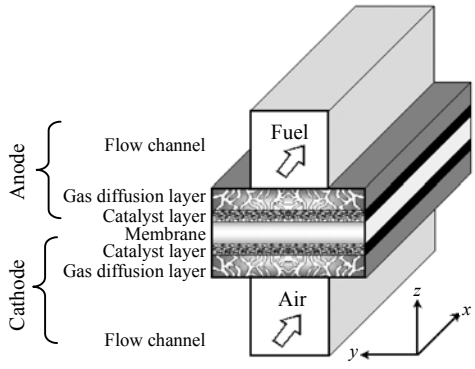

Fig.1 3D computational domain

Model equations

1. Gas flow channels

In the fuel cell channels, the gas-flow field is obtained by solving the steady-state Navier-Stokes equations, i.e. the continuity equation, the mass conservation equation for each phase yields the volume

fraction (r) and along with the momentum equations the pressure distribution inside the channels. The continuity equation for the gas phase inside the channel is given by

$$\nabla\cdot(r_{\mathrm{g}}\rho_{\mathrm{g}}\boldsymbol{u}_{\mathrm{g}})=0, \tag{1}$$

and for the liquid phase inside the channel becomes

$$\nabla\cdot(r_{\mathrm{l}}\rho_{\mathrm{l}}\boldsymbol{u}_{\mathrm{l}})=0, \tag{2}$$

where $\boldsymbol{u}$ is velocity vector (m/s), ρ is density (kg/m^3).

Two sets of momentum equations are solved in the channels, and they share the same pressure field. Under these conditions, it can be shown that the momentum equations become:

$$\begin{aligned}&\nabla\cdot(\rho_{\mathrm{g}}\boldsymbol{u}_{\mathrm{g}}\otimes\boldsymbol{u}_{\mathrm{g}}-\mu_{\mathrm{g}}\nabla\boldsymbol{u}_{\mathrm{g}})\\&\quad=-\nabla r_{\mathrm{g}}\left(P+\frac{2}{3}\mu_{\mathrm{g}}\nabla\cdot\boldsymbol{u}_{\mathrm{g}}\right)+\nabla\cdot[\mu_{\mathrm{g}}(\nabla\boldsymbol{u}_{\mathrm{g}})^{\mathrm{T}}],\end{aligned} \tag{3}$$

$$\begin{aligned}&\nabla\cdot(\rho_{\mathrm{l}}\boldsymbol{u}_{\mathrm{l}}\otimes\boldsymbol{u}_{\mathrm{l}}-\mu_{\mathrm{l}}\nabla\boldsymbol{u}_{\mathrm{l}})\\&\quad=-\nabla r_{\mathrm{l}}\left(P+\frac{2}{3}\mu_{\mathrm{l}}\nabla\cdot\boldsymbol{u}_{\mathrm{l}}\right)+\nabla\cdot[\mu_{\mathrm{l}}(\nabla\boldsymbol{u}_{\mathrm{l}})^{\mathrm{T}}],\end{aligned} \tag{4}$$

where P is pressure (Pa), μ is viscosity [kg/(m·s)].

The mass balance is described by the divergence of the mass flux through diffusion and convection. Multiple species are considered in the gas phase only, and the species conservation equation in multi-component, multi-phase flow can be written in the following expression for species i:

$$\begin{aligned}\nabla\cdot\Bigg[&-r_{\mathrm{g}}\rho_{\mathrm{g}}y_i\sum_{j=1}^{N}D_{ij}\frac{M}{M_j}\left[\left(\nabla y_j+y_j\frac{\nabla M}{M}\right)+(x_j-y_j)\frac{\nabla P}{P}\right]\\&+r_{\mathrm{g}}\rho_{\mathrm{g}}y_i\cdot\boldsymbol{u}_{\mathrm{g}}+\boldsymbol{D}_i^{\mathrm{T}}\frac{\nabla T}{T}\Bigg]=0,\end{aligned} \tag{5}$$

where T is temperature (K), y is mass fraction, x_i is mole fraction. Subscript i denotes oxygen at the cathode side and hydrogen at the anode side, and j is water vapour in both cases. Nitrogen is the third species at the cathode side.

The Maxwell-Stefan diffusion coefficients of any two species are dependent on temperature and pressure. They can be calculated according to the empirical relation based on kinetic gas theory (Fuller *et al*., 1966):

$$D_{ij}=\frac{T^{1.75}\times10^{-3}}{P\left[\left(\sum_k V_{ki}\right)^{1/3}+\left(\sum_k V_{kj}\right)^{1/3}\right]^2}\left[\frac{1}{M_i}+\frac{1}{M_j}\right]^{1/2}. \tag{6}$$

In Eq.(6), pressure P is in ($\times10^5$ Pa) and the binary diffusion coefficient D_{ij} is in (cm^2/s). The values for $\sum V_{ki}$ are given by Fuller *et al*.(1966).

The temperature field is obtained by solving the convective energy equation

$$\nabla\cdot[r_{\mathrm{g}}(\rho_{\mathrm{g}}Cp_{\mathrm{g}}\boldsymbol{u}_{\mathrm{g}}T-k_{\mathrm{g}}\nabla T)]=0, \tag{7}$$

where k is gases thermal conductivity [W/(m·K)].

The gas phase and the liquid phase are assumed to be in thermodynamic equilibrium; hence the temperature of the liquid water is the same as the gas phase temperature.

2. Gas diffusion layers

The physics of multiple phases through a porous medium is further complicated here with phase change and the sources and sinks associated with the electrochemical reaction. The equations used to describe transport in the gas diffusion layers are given below.

Mass transfer in the form of evaporation ($\dot{m}_{\mathrm{phase}}>0$) and condensation ($\dot{m}_{\mathrm{phase}}<0$) is assumed, so that the mass balance equations for both phases are:

$$\nabla\cdot[(1-sat)\rho_{\mathrm{g}}\varepsilon\boldsymbol{u}_{\mathrm{g}}]=\dot{m}_{\mathrm{phase}}, \tag{8}$$

$$\nabla\cdot(sat\,\rho_{\mathrm{l}}\varepsilon\boldsymbol{u}_{\mathrm{l}})=\dot{m}_{\mathrm{phase}}, \tag{9}$$

where sat is saturation, ε is porosity.

The momentum equation for the gas phase reduces to Darcy's law, which is, however, based on the relative permeability for the gas phase (KP). The relative permeability accounts for the reduction in pore space available for one phase due to the existence of the second phase (Berning and Djilali, 2003b).

The momentum equation for the gas phase inside

the gas diffusion layer becomes

$$\boldsymbol{u}_{\mathrm{g}} = -(1-sat)KP\nabla P/\mu_{\mathrm{g}}, \tag{10}$$

where KP is hydraulic permeability (m^2).

Two liquid water transport mechanisms are considered: shear, which drags the liquid phase along with the gas phase in the direction of the pressure gradient, and capillary forces, which drive liquid water from high to low saturation regions (Berning and Djilali, 2003b). Therefore, the momentum equation for the liquid phase inside the gas diffusion layer becomes

$$\boldsymbol{u}_{\mathrm{l}} = -\frac{KP_{\mathrm{l}}}{\mu_{\mathrm{l}}}\nabla P + \frac{KP_{\mathrm{l}}}{\mu_{\mathrm{l}}}\frac{\partial P_{\mathrm{c}}}{\partial sat}\nabla sat, \tag{11}$$

where P_{c} is capillary pressure (Pa).

The functional variation of capillary pressure with saturation is prescribed following Leverett (Berning and Djilali, 2003b) who showed that

$$P_{\mathrm{c}} = \sigma(\varepsilon/KP)^{1/2}[1.417(1-sat) - 2.12(1-sat)^2 + 1.263(1-sat)^3], \tag{12}$$

where σ is surface tension (N/m).

The liquid phase consists of pure water, while the gas phase has multi components. The transport of each species in the gas phase is governed by a general convection-diffusion equation in conjunction with the Stefan-Maxwell equations to account for multi species diffusion:

$$\nabla\cdot\left[-(1-sat)\rho_{\mathrm{g}}\varepsilon y_i\sum_{j=1}^{N}D_{ij}\frac{M}{M_j}\left[\left(\nabla y_j + y_j\frac{\nabla M}{M}\right) + (x_j - y_j)\frac{\nabla P}{P}\right] + (1-sat)\rho_{\mathrm{g}}\varepsilon y_i\cdot\boldsymbol{u}_{\mathrm{g}} + \varepsilon\boldsymbol{D}_i^{\mathrm{T}}\frac{\nabla T}{T}\right] = \dot{m}_{\mathrm{phase}}. \tag{13}$$

In order to account for geometric constraints of the porous media, the diffusivities are corrected using the Bruggemann correction formula (Nguyen *et al*., 2004):

$$D_{ij}^{\mathrm{eff}} = D_{ij}\times\varepsilon^{1.5}. \tag{14}$$

The heat transfer in the gas diffusion layers is governed by the energy equation as follows:

$$\nabla\cdot[(1-sat)(\rho_{\mathrm{g}}\varepsilon Cp_{\mathrm{g}}\boldsymbol{u}_{\mathrm{g}}T - k_{\mathrm{eff,g}}\varepsilon\nabla T)] = \varepsilon\beta(T_{\mathrm{solid}} - T) - \varepsilon\dot{m}_{\mathrm{phase}}\Delta H_{\mathrm{evap}}, \tag{15}$$

where k_{eff} is effective electrode thermal conductivity [W/(m·K)]; the term $[\varepsilon\beta(T_{\mathrm{solid}}-T)]$, on the right hand side, accounts for the heat exchange to and from the solid matrix of the GDL; β is a modified heat transfer coefficient that accounts for the convective heat transfer in [W/m^2] and the specific surface area [m^2/m^3] of the porous medium (Berning *et al*., 2002). Hence, the unit of β is [W/m^3], Cp is specific heat capacity [J/(kg·K)].

The gas phase and the liquid phase are assumed to be in thermodynamic equilibrium, i.e., the liquid water and the gas phase are at the same temperature.

The potential distribution in the gas diffusion layers is governed by:

$$\nabla\cdot(\lambda_{\mathrm{e}}\nabla\phi) = 0, \tag{16}$$

where λ_{e} is electrode electronic conductivity (S/m).

In order to account for the magnitude of phase change inside the GDL, expressions are required to relate the level of over- and under-saturation as well as the amount of liquid water present to the amount of water undergoing phase change.

In the case of evaporation, such relations must be dependent on (1) the level of under-saturation of the gas phase in each control volume and on (2) the surface area of the liquid water in the control volume. The surface area can be assumed proportional to the volume fraction of the liquid water in each cell. A plausible choice for the shape of the liquid water is droplets, especially since the catalyst area is Teflonated (Berning and Djilali, 2003b).

The evaporation rate of a droplet in a convective stream depends on the rate of undersaturation, the surface area of the liquid droplet, and a (diffusivity dependent) mass-transfer coefficient. The mass flux of water undergoing evaporation in each control volume can be represented by (Berning and Djilali, 2003b):

$$\dot{m}_{\mathrm{evap}} = M_{\mathrm{H_2O}}\varpi N_{\mathrm{D}}k_{\mathrm{xm}}\pi D_{\mathrm{drop}}\frac{x_{\mathrm{w0}} - x_{\mathrm{w}\infty}}{1 - x_{\mathrm{w0}}}. \tag{17}$$

where D_{drop} is diameter of droplet water (m), k_{xm} is Mass transfer coefficient [mol/(m^2·s)], M_{H_2O} is molecular weight of water (kg/mole).

The bulk concentration $x_{w\infty}$ is known by solving the continuity equation of water vapour. To obtain the concentration at the surface x_{w0}, it is reasonable to assume thermodynamic equilibrium between the liquid phase and the gas phase at the interface, i.e., the relative humidity of the gas in the immediate vicinity of the liquid is 100%. Under that condition, the surface concentration can be calculated based on the saturation pressure and is only a function of temperature.

The heat-transfer coefficient for convection around a sphere is well established, and by invoking the analogy between convective heat and mass transfer, the following mass-transfer coefficient was obtained by Berning and Djilali (2003b):

$$k_{xm}=\frac{c_{air}D_{H_2O}}{D_{drop}}\left[2+0.6\left(\frac{D_{drop}v_\infty\rho_g}{\mu_g}\right)^{1/2}\left(\frac{\mu_g}{\rho_g D_{H_2O}}\right)^{1/3}\right]. \tag{18}$$

It is further assumed that all droplets have a specified diameter D_{drop}, with the number of droplets in each control volume being found by dividing the total volume of the liquid phase in each control volume by the volume of one droplet:

$$N_D=\frac{6satV_{cv}}{\pi D_{drop}^3}. \tag{19}$$

In the case when the calculated relative humidity in a control volume exceeds 100%, condensation occurs and the evaporation term is disregarded.

The case of condensation is more complex, because it can occur on every solid surface area, but the rate of condensation can be different when it takes place on a wetted surface. In addition, the overall surface area in each control volume available for condensation shrinks with an increasing amount of liquid water present. Berning and Djilali (2003b) assumed that the rate of condensation depends only on the level of oversaturation of the gas phase multiplied by a condensation constant. Thus, the mass flux of water undergoing condensation in each control volume can be represented by:

$$\dot{m}_{cond}=\varpi C\frac{x_{w0}-x_{w\infty}}{1-x_{w0}}. \tag{20}$$

3. Catalyst layers

The catalyst layer is treated as a thin interface, where sink and source terms for the reactants are implemented. Due to the infinitesimal thickness, the source terms are actually implemented in the last grid cell of the porous medium. At the cathode side, the sink term for oxygen is given by:

$$S_{O_2}=-\frac{M_{O_2}}{4F}i_c, \tag{21}$$

where F is Faraday's constant (=96487 C/mole), i_c is cathode local current density (A/m^2), M_{O_2} is molecular weight of oxygen (kg/mole).

Whereas the sink term for hydrogen is specified as:

$$S_{H_2}=-\frac{M_{H_2}}{2F}i_a, \tag{22}$$

where i_a is anode local current density (A/m^2), M_{H_2} is molecular weight of hydrogen (kg/mole).

The production of water is modelled as a source term, and hence can be written as:

$$S_{H_2O}=\frac{M_{H_2O}}{2F}i_c. \tag{23}$$

The generation of heat in the cell is due to entropy changes as well as irreversibility's due to the activation overpotential (Lampinen and Fomino, 1993):

$$\dot{q}=\left[\frac{T(-\Delta s)}{n_e F}+\eta_{act,c}\right]i_c, \tag{24}$$

where n_e is number of electrons transfer, $\dot{q}$ is heat generation (W/m^2), η is overpotential (V).

The local current density distribution in the catalyst layers is modelled by the Butler-Volmer equation (Wang *et al*., 2003; Parthasarathy *et al*.,

1992):

$$i_{\mathrm{c}}=i_{\mathrm{o,c}}^{\mathrm{ref}}\left(\frac{C_{\mathrm{O_2}}}{C_{\mathrm{O_2}}^{\mathrm{ref}}}\right)\left[\exp\left(\frac{\alpha_{\mathrm{a}}F}{RT}\eta_{\mathrm{act,c}}\right)+\exp\left(-\frac{\alpha_{\mathrm{c}}F}{RT}\eta_{\mathrm{act,c}}\right)\right], \tag{25}$$

$$i_{\mathrm{a}}=i_{\mathrm{o,a}}^{\mathrm{ref}}\left(\frac{C_{\mathrm{H_2}}}{C_{\mathrm{H_2}}^{\mathrm{ref}}}\right)^{1/2}\left[\exp\left(\frac{\alpha_{\mathrm{a}}F}{RT}\eta_{\mathrm{act,a}}\right)+\exp\left(-\frac{\alpha_{\mathrm{c}}F}{RT}\eta_{\mathrm{act,a}}\right)\right], \tag{26}$$

where $C_{\mathrm{H_2}}$ is local hydrogen concentration (mole/m^3), $C_{\mathrm{H_2}}^{\mathrm{ref}}$ is reference hydrogen concentration (mole/m^3), $C_{\mathrm{O_2}}$ is local oxygen concentration (mole/m^3), $C_{\mathrm{O_2}}^{\mathrm{ref}}$ is reference oxygen concentration (mole/m^3), C_{p} is specific heat capacity [J/(kg·K)], D is diffusion coefficient (m^2/s), $i_{\mathrm{o,a}}^{\mathrm{ref}}$ is anode reference exchange current density, $i_{\mathrm{o,c}}^{\mathrm{ref}}$ is cathode reference exchange current density, R is universal gas constant (=8.314 J/(mole·K)), s is specific entropy [J/(mole·K)], α_{a} is charge transfer coefficient, anode side, and α_{c} is charge transfer coefficient, cathode side.

4. Membrane

The balance between the electro-osmotic drag of water from anode to cathode and back diffusion from cathode to anode yields the net water flux through the membrane:

$$N_{\mathrm{w}}=n_{\mathrm{d}}M_{\mathrm{H_2O}}\frac{i}{F}-\nabla\cdot(\rho D_{\mathrm{w}}\nabla c_{\mathrm{w}}), \tag{27}$$

where N_{w} is net water flux across the membrane (kg/m^2·s), n_{d} is electro-osmotic drag coefficient.

The water diffusivity in the polymer can be calculated as follow (Siegel *et al*., 2004):

$$D_{\mathrm{w}}=1.3\times10^{-10}\exp\left[2416\left(\frac{1}{303}-\frac{1}{T}\right)\right]. \tag{28}$$

The variable c_{w} represents the number of water molecules per sulfonic acid group (i.e. mol H_2O/equivalent SO_3^{-1}). The water content in the electrolyte phase is related to water vapour activity via (Hu *et al*., 2004a; 2004b):

$$\begin{aligned} &c_{\mathrm{w}}=0.043+17.81a-39.85a^2+36.0a^3,\ 0<a\leq1;\\ &c_{\mathrm{w}}=14.0+1.4(a-1),\qquad 1<a\leq3;\\ &c_{\mathrm{w}}=16.8,\qquad a\geq3. \end{aligned} \tag{29}$$

The water vapour activity a is given by:

$$a=x_{\mathrm{w}}P/P_{\mathrm{sat}}. \tag{30}$$

For heat transfer purposes, the membrane is considered as a conducting solid, which means that the transfer of energy associated with the net water flux through the membrane is neglected. Heat transfer in the membrane is governed by:

$$\nabla\cdot(k_{\mathrm{mem}}\cdot\nabla T)=0, \tag{31}$$

where k_{mem} is membrane thermal conductivity [W/(m·K)].

The potential loss in the membrane is due to resistance to proton transport across the membrane, and is governed by:

$$\nabla\cdot(\lambda_{\mathrm{m}}\nabla\phi)=0, \tag{32}$$

where λ_{m} is membrane ionic conductivity (S/m).

5. Cell potential

Useful work (electrical energy) is obtained from a fuel cell only when a current is drawn, but the actual cell potential (E_{cell}) is decreased from its equilibrium thermodynamic potential (E) because of irreversible losses. The cell potential is obtained by subtracting all overpotentials (losses) from the equilibrium thermodynamic potential as in the following expression (Bernardi and Verbrugge, 1992; Gurau *et al*., 1998):

$$E_{\mathrm{cell}}=E-\eta_{\mathrm{act}}-\eta_{\mathrm{ohm}}-\eta_{\mathrm{mem}}-\eta_{\mathrm{Diff}}. \tag{33}$$

The equilibrium potential is determined using the Nernst equation (Springer *et al*., 1991):

$$\begin{aligned} E=&1.229-0.83\times10^{-3}(T-298.15)\\ &+4.3085\times10^{-5}T[\ln(P_{\mathrm{H_2}})+\ln(P_{\mathrm{O_2}})/2]. \end{aligned} \tag{34}$$

The anode and cathode activation overpotentials are calculated from Butler-Volmer Eqs.(25) and (26). The ohmic overpotentials in GDLs and protonic

overpotential in membrane are calculated from the potential Eqs.(16) and (31) respectively.

The anode and cathode diffusion overpotentials are calculated from the following equations (Hirschenhofer *et al*., 2002):

$$\eta_{\mathrm{Diff,c}}=\frac{RT}{2F}\ln\left(1-\frac{i_{\mathrm{c}}}{i_{\mathrm{L,c}}}\right), \tag{35}$$

$$\eta_{\mathrm{Diff,a}}=\frac{RT}{2F}\ln\left(1-\frac{i_{\mathrm{a}}}{i_{\mathrm{L,a}}}\right), \tag{36}$$

$$i_{\mathrm{L,c}}=\frac{2FD_{\mathrm{O_2}}C_{\mathrm{O_2}}}{\delta_{\mathrm{GDL}}}, \tag{37}$$

$$i_{\mathrm{L,a}}=\frac{2FD_{\mathrm{H_2}}C_{\mathrm{H_2}}}{\delta_{\mathrm{GDL}}}. \tag{38}$$

Boundary conditions

Boundary conditions have to be applied for all variables of interest in the computational domain. In order to reduce computational cost, the geometric periodicity of the cell is taken advantage of. Hence symmetry is assumed in the *y*-direction, i.e. all gradients in the *y*-direction are set to zero at the *x*-*z* plane boundaries of the domain. With the exception that at the channel inlets and outlets, a zero flux condition is applied at all *x*-boundaries (*y*-*z* planes).

The inlet values at the anode and cathode are prescribed for the velocity, temperature and species concentrations (Dirichlet boundary conditions). The gas streams entering the cell are fully humidified, but no liquid water is contained in the gas stream. The inlet velocities of air and fuel are calculated based on the desired current density according to:

$$u_{\mathrm{in,c}}=\zeta_{\mathrm{c}}\frac{I}{4F}A_{\mathrm{MEA}}\frac{1}{x_{\mathrm{O_2,in}}}\frac{RT_{\mathrm{in,c}}}{P_{\mathrm{c,in}}}\frac{1}{A_{\mathrm{ch}}}, \tag{39}$$

$$u_{\mathrm{in,a}}=\zeta_{\mathrm{a}}\frac{I}{2F}A_{\mathrm{MEA}}\frac{1}{x_{\mathrm{H_2,in}}}\frac{RT_{\mathrm{in,a}}}{P_{\mathrm{a,in}}}\frac{1}{A_{\mathrm{ch}}}, \tag{40}$$

where A_{MEA} is geometrical area of membrane electrode assembly (m^2), A_{ch} is cross sectional area of flow channel (m^2), I is cell operating current density ($\mathrm{A/m}^2$).

At the outlets of the gas-flow channels, only the pressure is prescribed as the desired electrode pressure; for all other variables, the gradient in the flow direction (*x*) is assumed to be zero (Neumann boundary conditions).

At the external surfaces in the *z*-direction, (top and bottom surfaces of the cell), temperature is specified and zero heat flux is applied at the *x*-*y* plane of the conducting boundary surfaces. Combinations of Dirichlet and Neumann boundary conditions are used to solve the electronic and protonic potential equations. Dirichlet boundary conditions are applied at the land area. Neumann boundary conditions are applied at the interface between the gas channels and the gas diffusion layers to give zero potential flux into the gas channels. Similarly, the protonic potential field requires a set of potential boundary condition and zero flux boundary condition at the anode catalyst layer interface and cathode catalyst layer interface respectively.

SOLUTION ALGORITHM

The governing equations were discretized using a finite volume method and solved using a general-purpose computational fluid dynamic code. Stringent numerical tests were performed to ensure that the solutions were independent of the grid size. A computational mesh of 15×10^4 computational cells was found to provide sufficient spatial resolution. The solution begins by specifying a desired current density of the cell to use for calculating the inlet flow rates at the anode and cathode sides. An initial guess of the activation overpotential is obtained from the desired current density using the Butler-Volmer equation. Then followed by computing the flow fields for each phase for velocities *u*, *v*, *w*, and pressure *P*. Once the flow field is obtained, the mass fraction equations are solved for the mass fractions of oxygen, hydrogen, nitrogen, and water. Scalar equations are solved last in the sequence of the transport equations for the temperature field in the cell and potential fields in the gas diffusion layers and the membrane. The local current densities are solved based on the Butler-Volmer equation. After the local current densities are obtained, the local activation overpotentials can be readily calculated from the Butler-Volmer equation. The local activation overpotentials are updated after each global iterative loop. Convergence

criteria are then applied on each variable and the procedure is repeated until convergence. The properties are updated after each global iterative loop based on the new local gas composition and temperature. Source terms reflect changes in the overall gas phase mass flow due to consumption or production of gas species via reaction and due to mass transfer between water in the vapour phase and water in the liquid phase or dissolved in the polymer (phase-change).

The strength of the current model is clearly to perform parametric studies and explore the impact of various parameters on the transport mechanisms and on fuel cell performance. The flow diagram of the algorithm is shown in Fig.2.

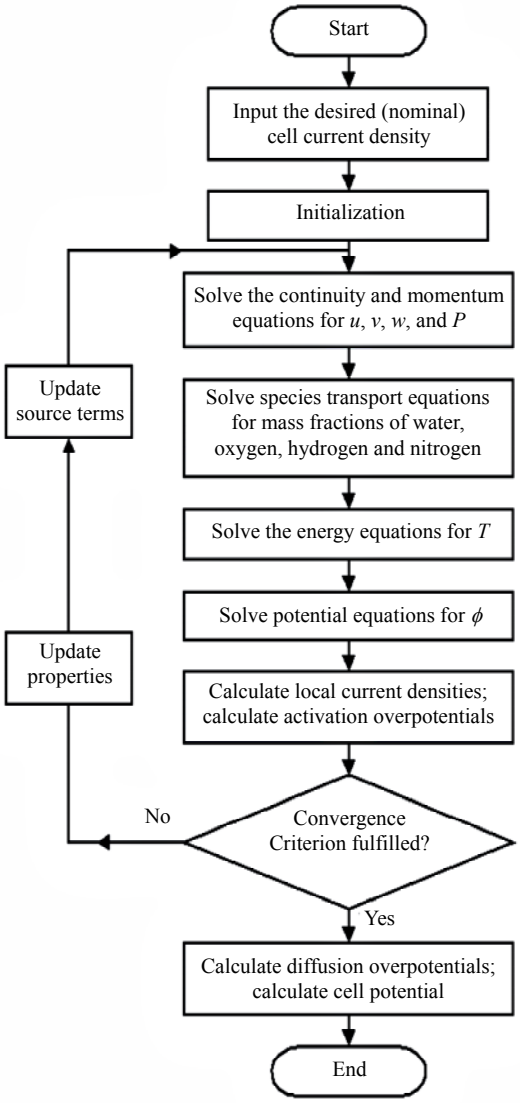

Fig.2 Flow diagram of the solution procedure used

RESULTS AND DISCUSSION

Model accuracy validation

The multi-phase model is validated by comparing model results to experimental data provided by Wang *et al*.(2003). The values of the electrochemical transport parameters for the base case operating conditions are listed in Table 1. The geometric and the base case operating conditions are listed in Table 2.

It is important to note that because this model accounts for all major transport processes and the modelling domain involves all the elements of a complete cell, no parameters needed to be adjusted in order to obtain physical results.

Fig.3 shows the comparison of the polarization curves from the experimental data with the values obtained by the model at different operating fuel cell temperatures. It can be seen that the modelling results compare well with the experimental data. The importance of phase change to the accurate modelling of fuel cell performance is illustrated. Performance curves with and without phase change are also shown in Fig.3 for the base case conditions. Comparison of the two curves demonstrates that the effects of liquid water accumulation become apparent even at relatively low values of current density. Furthermore, when liquid water effects are not included in the model, the cell voltage dose not exhibit an increasingly steep drop as the cell approaches its limiting current density. This drop off in performance is clearly demonstrated by experimental data, but cannot be accurately modelled without the incorporation of phase change. By including the effects of phase change, the current model is able to more closely simulate performance, especially in the region where mass transport effects begin to dominate.

Optimization study

The performance of fuel cells is affected by operating point (cell voltage and related current density), operating parameters, design parameters, and material parameters. Operating conditions that give optimal fuel cell performance depend on the application area. Stationary, portable, and transportation applications all have different requirements and operate in different environments. What all this means is that the

Table 1 Electrode and membrane parameters for base operating conditions

Parameter	Symbol	Value	Unit	Reference
Electrode porosity	ε	0.4	–	Bernadi and Verbrugge, 1992
Electrode electronic conductivity	λ_e	100	S/m	Sivertsen and Djilali, 2005
Membrane ionic conductivity (humidified Nafion® 117)	λ_m	17.1223	S/m	Bernadi and Verbrugge, 1992
Transfer coefficient, anode side	α_a	0.5	–	Gurau *et al*., 1998
Transfer coefficient, cathode side	α_c	1	–	Parthasarathy *et al*., 1992
Cathode reference exchange current density	$i_{o,c}^{ref}$	1.8081E−3	A/m^2	Berning and Djilali, 2003a
Anode reference exchange current density	$i_{o,a}^{ref}$	2465.598	A/m^2	Berning and Djilali, 2003a
Electrode thermal conductivity	k_{eff}	1.3	W/(m·K)	Nguyen *et al*., 2004
Membrane thermal conductivity	k_{mem}	0.455	W/(m·K)	Nguyen *et al*., 2004
Electrode hydraulic permeability	k_p	1.76E−11	m^2	Wang *et al*., 2003
Entropy change of cathode side reaction	ΔS	−326.36	J/(mole·K)	Lampinen and Fomino, 1993
Heat transfer coefficient between solid and gas phase	β	4E+6	W/m^3	Berning *et al*., 2002
Protonic diffusion coefficient	D_{H^+}	4.5E−9	m^2/s	Bernadi and Verbrugge, 1992
Fixed-charge concentration	c_f	1200	mole/m^3	Bernadi and Verbrugge, 1992
Fixed-site charge	z_f	−1	–	Bernadi and Verbrugge, 1992
Electro-osmotic drag coefficient	n_d	2.5	–	Springer *et al*., 1991
Droplet diameter	D_{drop}	1.0×10^{-8}	m	Berning and Djilali, 2003b
Condensation constant	C	1.0×10^{-5}	–	Berning and Djilali, 2003b
Scaling parameter for evaporation	ϖ	0.01	–	Berning and Djilali, 2003b

Table 2 Geometrical and operational parameters for base case conditions

Parameter	Symbol	Value	Unit
Channel length	L	0.05	m
Channel width	W	1E−3	m
Channel height	H	1E−3	m
Land area width	W_{land}	1E−3	m
Gas diffusion layer thickness	δ_{GDL}	0.26E−3	m
Wet membrane thickness (Nafion® 117)	δ_{mem}	0.23E−3	m
Catalyst layer thickness	δ_{CL}	0.0287E−3	m
Hydrogen reference mole fraction	$x_{H_2}^{ref}$	0.84639	–
Oxygen reference mole fraction	$x_{O_2}^{ref}$	0.17774	–
Anode pressure	P_a	3	$\times10^5$ Pa
Cathode pressure	P_c	3	$\times10^5$ Pa
Inlet fuel and air temperature	T_{cell}	353.15	K
Relative humidity of inlet fuel and air (fully humidified conditions)	ψ	100	%
Air stoichiometric flow ratio	ξ_c	2	–
Fuel stoichiometric flow ratio	ξ_a	2	–

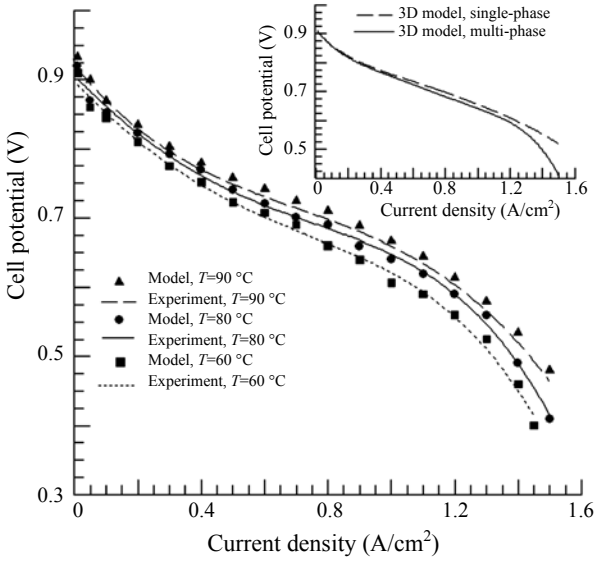

Fig.3 comparison of 3D simulation with an experimental polarization curve

present 3D model can make it fast and easy to try all sorts of combinations of geometries, materials, and operating conditions to come up with an optimum design for the application.

1. Optimum operating point for the cell

Usually, compromises in the operating points (cell voltages and related current densities) of the specific cell are necessary to meet the application requirements, obtain lowest system cost, and achieve acceptable cell life. Operating points are based on defining specific system requirements, such as power level, voltage, efficiency, and system weight. It is a matter of selecting a cell operating point (cell voltage and related current density) until the system requirements are satisfied (such as lowest cost, lightest unit, and highest power density or such as highest efficiency and lowest operating cost). For example, a design point at high current density will allow a smaller cell size at lower capital cost to be used for the stack, but a lower system efficiency results (because of the lower cell voltage) and attendant higher operating cost. This type of operating point would be typified by a portable application (such as vehicle, laptop PC, or cell phone) where light weight and small volume are important drivers for cost effectiveness. Operating at a lower current density, but higher voltage (higher efficiency, and lower operating cost) would be more suitable for stationary power plant operation.

Fig.4 shows the relationship between the thermodynamic efficiency and the power density of the cell operating at base case conditions. Also, Fig.4 shows the variation of the maximum temperature gradient inside the cell with cell power density. It is clearly shown that the efficiency at maximum power is much lower than the efficiency at partial loads, which makes the fuel cells very attractive and efficient for applications with highly variable loads where most of the time the fuel cell is operated at low load and high efficiency. The cell's nominal efficiency is therefore an arbitrary value, ranging anywhere between about 0.4 and ~0.7, which can be selected for any cell based on economic rather than on physical constraints. For example, for a cell operating at base case condition, one may select a maximum operating point at 0.56 V and 1.25 A/cm^2, resulting in 0.7 W/cm^2 and efficiency of 0.455 with maximum temperature gradient 7.9 K inside the cell. However, one may get the same power output by selecting two cells, connected in series, operating at 0.733 V and 0.5 A/cm^2 each. Obviously, the latter would be twice as expensive, heavy, and large, but would be more efficient (0.584), and therefore would consume less fuel. Also, the latter two series cells runs with less temperature rise inside each cell (only 2.73 K), and this leads to prevention of drying out of the membrane and excessive thermal stresses that may result in rupture of the membrane, and therefore less thermal management problems, and achieve long cell life.

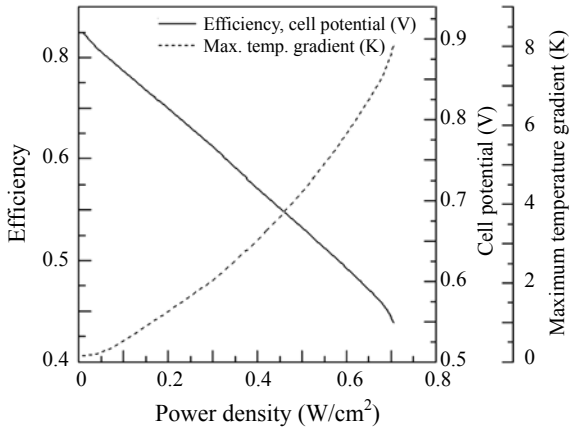

Fig.4 Relationship between the thermodynamic efficiency and the power density of the cell operates at base case conditions

However, since efficiency drops with increasing power density, there is a trade-off between high power and high efficiency. Fuel cell designers must select the desired operating range according to whether efficiency or power is paramount for the given application.

For an optimum fuel cell performance, and in order to avoid large thermal stresses, it is desirable to achieve uniform temperature distribution gradients inside the fuel cell to preventing failure. The temperature distributions inside the cell for the above example (current 0.5 A/cm^2 and 1.25 A/cm^2) are shown in Fig.5. In general, the temperature at the cathode side is higher than at the anode side, due to the reversible and irreversible entropy production. Naturally, the maximum temperature occurs, where the electrochemical activity is highest, which is near the cathode side inlet area. The temperature peak appears in the cathode catalyst layer, implying that major heat generation takes place in this region. The low load condition of 0.5 A/cm^2 results in more even distribution of the temperature distribution inside the cell due to the more even distribution of the molar oxygen fraction at the catalyst layer results in more even distribution of the local current density. This is different for high load condition of 1.25 A/cm^2. A much larger fraction of the current is being generated near the inlet of the cathode side at the catalyst layer and this leads to a significantly larger amount of heat being generated here.

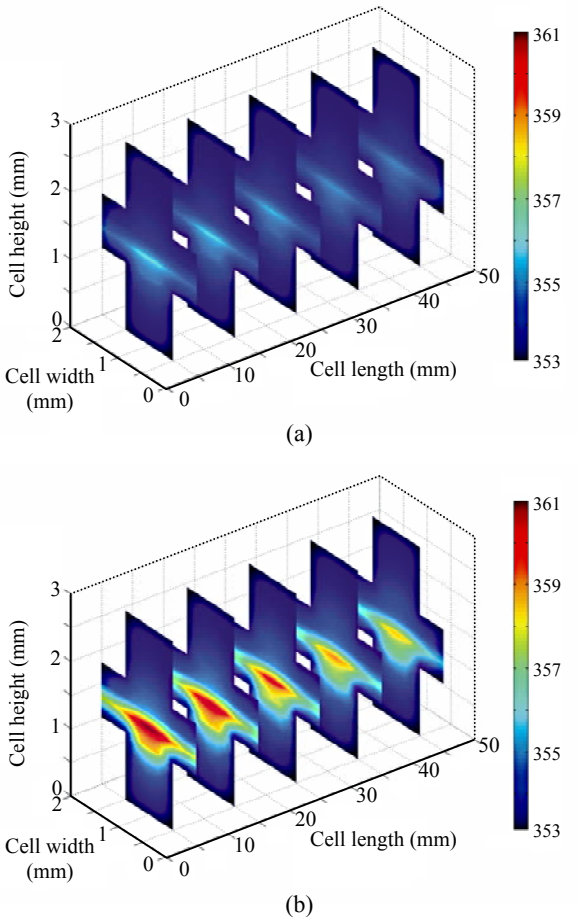

Fig.5 Temperature distributions in the cell for two different nominal current densities
(a) 0.5 A/cm^2; (b) 1.25 A/cm^2

2. Optimum cell performance

In designing a cell, everything comes into play: cell potential, cell life, the pressure of the gas in the anode and cathode, operating temperature, the required mass flow of the reactants, indicating how much water is in the fuel and the oxidant, material of various elements, and even the dimensions of various elements, key among them being the membrane, gas diffusion layers, and the gas channels. Changing the cell operating parameters can have either a beneficial or a detrimental impact on fuel cell performance. The material parameters, cell design, and cell operating conditions that give optimal performance depend on the application area. Stationary, portable, and transportation applications all have different requirements, operate in different environments, and the available fuel and oxidant conditions vary greatly. A PEM fuel cell used in a stationary application could operate from fully humidified fuel with high operating temperature and benefit from a compressor to increase air pressure, which increases the cell's power output. In contrast, a fuel cell in portable applications such as laptop PC or cell phone would most likely operate with air at atmospheric conditions. Furthermore, the amount of water available for fuel and air humidification in a portable fuel cell might be limited. Other requirements vary by application. For example, fuel cell weight is much more critical in mobile appliances, and it limits the choice of materials for manufacturing. In order to determine the optimum cell performance, the cell power at various operating conditions is compared at constant nominal current density.

The performance characteristics of the fuel cell based on a certain parameter can be obtained by varying that parameter while keeping all other parameters constant. Results obtained from these pa-

rametric studies will allow us to identify the critical parameters for fuel cell performance. Results with different operating conditions for the cell operating at nominal current density of 1.2 A/cm^2 are presented in Fig.6.

The cell potential with all losses resulting from the base case and various operating conditions are shown in Fig.6a. In general, the most significant contributor to potential loss for the cell is the cathode catalyst layer. A low permeability and exchange current density combine to demand a significant portion of the reaction free energy. The membrane layer shows sizable potential loss due to low ionic conductivity compared to gas diffusion layer. The loss in the anode catalyst layer is insignificant due to the relatively high permeability of the hydrogen and, more importantly, because the anode reaction is orders of magnitude faster than the cathode for a given activation overpotential.

The activation overpotential decreases with increasing of cell operating temperature (Case 3). This is because the exchange current density of the oxygen reduction reaction increases rapidly with temperature due to the enhanced reaction kinetics, which reduces activation losses. A higher temperature leads also to a higher diffusivity of the hydrogen protons in the electrolyte membrane, thereby reducing the membrane resistance and this leads to reducing the potential loss in the membrane. Mass transport loss increases as the cell operating temperature increases due to the reduction of the molar oxygen fraction in the incoming gas streams and, hence, a reduction in the molar oxygen fraction at the catalyst layer.

The activation overpotential decreases with increasing cell operating pressure (Case 5). This is because the exchange current density of the oxygen

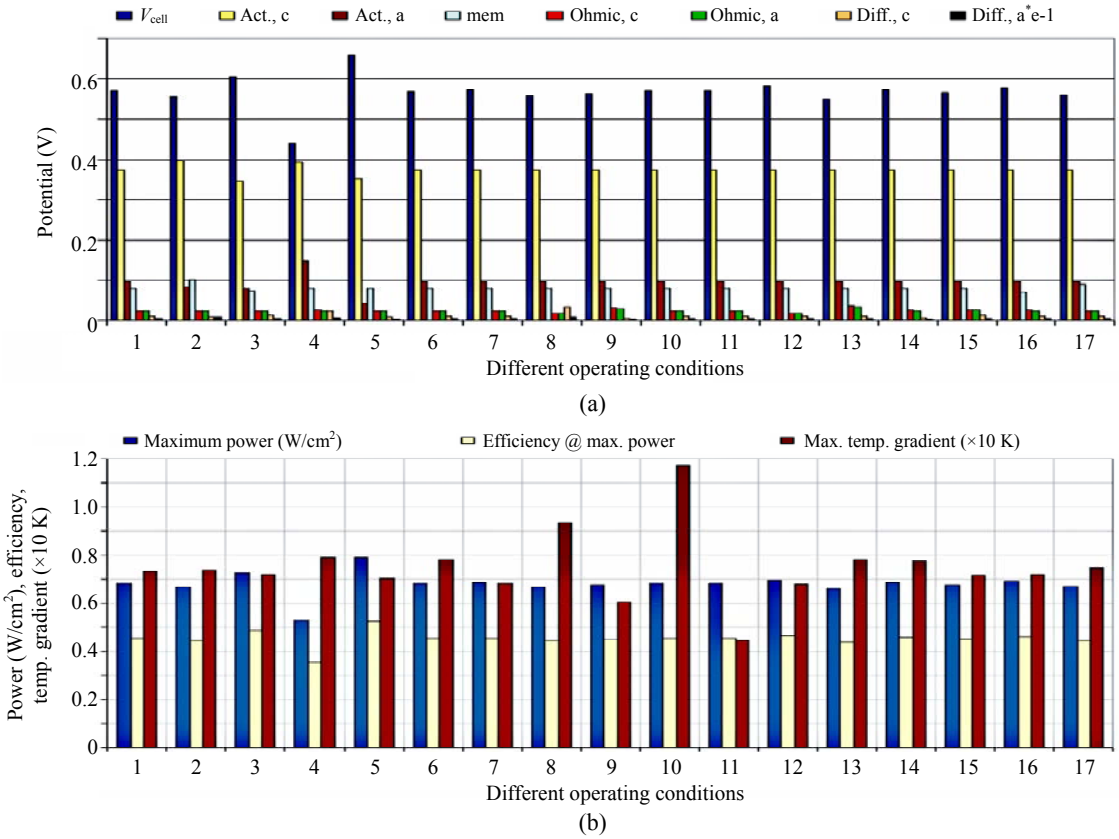

Fig.6 (a) Cell potential with different losses for different operating conditions; (b) Optimum power with corresponding efficiency and temperature gradient for different operating conditions

1: Base case; 2: Cell operating temperature=60 °C; 3: Cell operating temperature=90 °C; 4: Cell operating pressure=1×10^5 Pa; 5: Cell operating pressure=5×10^5 Pa; 6: Stoichiometric flow ratio=1.5; 7: Stoichiometric flow ratio=3; 8: GDL porosity=0.3; 9: GDL porosity=0.5; 10: GDL thermal conductivity=0.5 W/(m·K); 11: GDL thermal conductivity=2.9 W/(m·K); 12: Gas channel width=0.8 mm; 13: Gas channel width=1.2 mm; 14: GDL thickness=0.2 mm; 15: GDL thickness=0.3 mm; 16: Membrane thickness=0.2 mm; 17: Membrane thickness=0.26 mm; V_{cell}: cell potential; Act.: Activation overpotential; mem.: membrane overpotential; ohmic: ohmic overpotential; diff.: diffusion overpotential; the suffix "c" and "a" for cathode and anode respectively; Efficiency @ max. power: fuel cell efficiency at maximum power

reduction reaction increases with increasing of the cell operating pressure due to the enhanced reaction kinetics. To reduce mass transport loss, the cathode is usually run at high pressure. In essence, higher pressures help to force the oxygen and hydrogen into contact with the electrolyte and this leads to reducing the mass transport loss.

Higher gas diffusion layer porosity improves the mass transport within the cell and this leads to reducing the mass transport loss (Case 9). Another loss mechanism that is important when considering different gas diffusion layer porosities is the contact resistance. Contact resistance occurs at all interfaces inside the fuel cell. The magnitude of the contact resistance depends on various parameters such as the surface material and treatment and the applied stack pressure. The electrode porosity has a negative effect on electron conduction, since the solid matrix of the gas diffusion layer provide the pathways for electron transport, the higher volume porosity increases resistance to electron transport in the gas diffusion layers.

A reduced width of the land area increases the contact resistance between the bipolar plates and the gas diffusion electrodes (Case 13). Since this is an ohmic loss, it is directly correlated to the land area width (Cases 12 and 13).

The effect of gas diffusion layer thickness on the fuel cell performance is mostly on the mass transport, as the ohmic losses of the electrons inside the gas diffusion layer are relatively small due to the high conductivity of the carbon fibber paper. A thinner gas diffusion layer increases the mass transport through it, and this leads to reduction the mass transport loss (Case 14).

The effect of membrane thickness on the fuel cell performance is mostly on the resistance of the proton transport across the membrane (Cases 16 and 17). The potential loss in the membrane is due to resistance to proton transport across the membrane from anode catalyst layer to cathode catalyst layer. Therefore, a reduction in the membrane thickness means that the path travelled by the protons will be decreased; thereby reducing the membrane resistance and this leads to reducing the potential loss in the membrane, which in turn leads to less heat generation in the membrane.

The optimum power with corresponding efficiency and temperature gradient for different operating conditions are shown in Fig.6b. Higher operating temperature (Case 3) will increase cell power and then cell efficiency and lower cost. In addition, the maximum temperature gradient inside the cell will reduce. The molar oxygen fraction at the catalyst layer decreases with increasing cell operating temperature, due to the reduction of the molar oxygen fraction in the incoming gas streams. The result is a much higher fraction of the local current density and it is generated under the channel area. Therefore, the maximum temperature occurs at higher cell operating temperature (Case 3), but the maximum temperature gradient appears in the lower cell operating temperature (Case 2), due to the high activation overpotential, which leads to more heat generation with drop of the cell voltage.

Operating at a higher pressure (Case 5) will increase cell power and efficiency and lower cost. In addition, the maximum temperature gradient inside the cell will decrease. However, there will be a higher parasitic power to compress the reactants and the cell stack pressure vessel and piping will have to withstand the greater pressure. This adds cost. The effect of the cell operating pressure on the local current distribution shows that the higher cell operating pressure results in more even distribution of the local current density due to the high oxygen concentration at the catalyst layer. This leads to the fact that for a lower cell operating pressure at a constant nominal current density, there is a much stronger distribution of current inside the cell, with the maximum local current density being at the inlet under the channel area. Therefore, the maximum temperature gradient appears in the cathode side catalyst layer of the lower cell operating pressure (Case 4).

Operating at a higher stoichiometric flow ratio (Case 7) will increase cell power and efficiency and lower cost. In addition, the maximum temperature gradient inside the cell will decrease. However, there is a cost to pay for an increase in the stoichiometric flow ratio; there must be an optimum, where the gain in the cell performance just balances the additional costs of a more powerful blower. This will have to be carefully considered, when designing the fuel cell system. The effect of the stoichiometric flow ratio on the local current distribution shows that the higher stoichiometric flow ratio results in more even distri-

bution of the local current density due to the high oxygen concentration at the catalyst layer. Therefore, the maximum temperature gradient appears in the cathode side catalyst layer of the lower stoichiometric flow ratio (Case 6).

Operating at lower or higher gas diffusion layer porosities from the base case value (Cases 8 and 9) will decrease cell power and efficiency, but with higher porosity value (Case 9); the maximum temperature gradient inside the cell will decrease. For a lower value of the porosity a much higher fraction of the total current is generated under the channel area (Case 8). This can lead to local hot spots inside the membrane electrode assembly. These hot spots can lead to further drying out of the membrane, thus increasing the electric resistance, which in turn leads to more heat generation and can lead to a failure of the membrane.

Operating at a higher gas diffusion layer thermal conductivity (Case 11) will decrease the maximum temperature gradient inside the cell. The cell power and efficiency remains constant with both case of higher and lower values of thermal conductivity. The maximum temperature with higher gradient appears in the cathode side catalyst layer of lower thermal conductivity (Case 10). Heat generated in the catalyst layer is primarily removed through the gas diffusion layer to the current collector rib by lateral conduction. This process is controlled by the gas diffusion later thermal conductivity. Therefore, the membrane temperature is strongly influenced by the gas diffusion layer thermal conductivity, indicating a significant role played by lateral heat conduction through the gas diffusion layer in the removal of waste heat to the ambient environment. Therefore, a gas diffusion layer material having higher thermal conductivity is strongly recommended for fuel cells designed to operate with high power.

Operating at a narrow gas flow channel (Case 12) will increase cell power and efficiency and lower cost. In addition, the maximum temperature gradient inside the cell will decrease. However, the pressure drop inside the cell will increase with a narrow gas flow channel. The temperature peak appears in the cathode side catalyst layer of the wider channel (Case 13), implying that major heat generation takes place where the electrochemical activity is highest. This is because of the increase in the width of the gas flow channel means that the velocity of the incoming gas has to be decreased with all remaining parameters remaining constant, and this will decrease the gases velocity in the gas diffusion layer and hence, reduce the convection heat transfer in this region.

Operating with a thinner gas diffusion layer (Case 14) will slightly increase cell power and efficiency and lower cost. However, the maximum temperature gradient inside the cell will increase. The thicker gas diffusion layer results in more even distribution of the local current density due to the more even distribution of the molar oxygen fraction at the catalyst layer (Case 15).

Operating with a thinner membrane (Case 16) will increase cell power and efficiency and lower cost. In addition, the maximum temperature gradient inside the cell will decrease due to reducing the potential loss in the membrane.

CONCLUSION

A full 3D, multi-phase computational fluid dynamics model of a PEM fuel cell with straight flow channels has been developed. The model was developed to improve fundamental understanding of transport phenomena in PEM fuel cells and to investigate the impact of various operation parameters on performance. This comprehensive model accounts for the major transport phenomena in a PEM fuel cell: convective and diffusive heat and mass transfer, electrode kinetics, transport and phase change mechanism of water, and potential fields. The model accounts for the liquid water flux inside the gas diffusion layers by viscous and capillary forces and hence is capable of predicting the amount of liquid water inside the gas diffusion layers. The physics of phase change are included in this model by prescribing the local evaporation term as a function of the amount of liquid water present and the level of undersaturation, whereas the condensation is modeled as a function of the level of oversaturation. Optimization study using this model has been performed. The study quantifies the impact of operating, design, and material parameters on fuel cell performance. The model is shown to be able to: (1) gain understanding of the many interacting, complex electrochemical and transport phenomena that cannot be studied experi-

mentally; (2) identify limiting steps and components; and (3) provide a computer-aided tool for design and optimization of future fuel cell with much higher power density and lower cost. In addition, the results showed that the model is capable of identifying important parameters for the wetting behaviour of the gas diffusion layers and can be used to identify conditions that might lead to the onset of pore plugging, which has detrimental effect on the fuel cell performance, especially in the mass transport limited region.

References

Bernardi, D.M., Verbrugge, M.W., 1992. A mathematical model of the solid-polymer-electrolyte fuel cell. *J. Electrochem. Soc.*, **139**(9):2477-2491. [doi:10.1149/1.2221251]

Berning, T., Djilali, N., 2003a. 3D computational analysis of transport phenomenon in a PEM fuel cell–A parametric study. *J. Power Sources*, **124**(2):440-452. [doi:10.1016/S0378-7753(03)00816-4]

Berning, T., Djilali, N., 2003b. A 3D, multi-phase, multi-component model of the cathode and anode of a PEM fuel cell. *J. Electrochem. Soc.*, **150**(12):A1589-A1598. [doi:10.1149/1.1621412]

Berning, T., Lu, D.M., Djilali, N., 2002. 3D computational analysis of transport phenomena in a PEM fuel cell. *J. Power Sources*, **106**(1-2):284-294. [doi:10.1016/S0378-7753(01)01057-6]

Coppo, M., Siegelb, N.P., von Spakovskyc, M.R., 2005. On the influence of temperature on PEM fuel cell operation. *J. Power Sources*, **159**(1):560-569. [doi:10.1016/j.jpowsour.2005.09.069]

Fuller, E.N., Schettler, P.D., Giddings, J.C., 1966. A new methode for prediction of binary gas-phase diffusion coefficients. *Ind. Eng. Chem.*, **58**(5):18-27. [doi:10.1021/ie50677a007]

Gurau, V., Liu, H., Kakac, S., 1998. 2D model for proton exchange membrane fuel cells. *AIChE Journal*, **44**(11):2410-2422. [doi:10.1002/aic.690441109]

Hirschenhofer, J.H., Stauffer, D.B., Engleman, R.R., Klett, M.G., 2002. Fuel Cell Handbook, DOE/NETL-2002/1179 (DE-AM26-99FT40575), U.S. Department of Fossil Energy, Morgantown Energy Technology Center, Morgantown, WV, Chapter 2, p.11-12.

Hu, M., Gu, A., Wang, M., Zhu, X., Yu, L., 2004a. Three dimensional, two phase flow mathematical model for PEM fuel cell. Part I. Model development. *Energy Conversion Manage*, **45**(11-12):1861-1882. [doi:10.1016/j.enconman.2003.09.022]

Hu, M., Gu, A., Wang, M., Zhu, X., Yu, L., 2004b. Three dimensional, two phase flow mathematical model for PEM fuel cell. Part II. Analysis and discussion of the internal transport mechanisms. *Energy Conversion and Management*, **45**(11-12):1883-1916. [doi:10.1016/j.enconman.2003.09.023]

Ju, H., Meng, H., Wang, C.Y., 2005. A single-phase, non-isothermal model for PEM fuel cells. *Int. J. Heat and Mass Transfer*, **48**(7):1303-1315. [doi:10.1016/j.ijheatmasstransfer.2004.10.004]

Lampinen, M.J., Fomino, M., 1993. Analysis of free energy and entropy changes for half-cell reactions. *J. Electrochem. Soc.*, **140**(12):3537-3546. [doi:10.1149/1.2221123]

Nguyen, P.T., Berning, T., Djilali, N., 2004. Computational model of a PEM fuel cell with serpentine gas flow channels. *J. Power Sources*, **130**(1-2):149-157. [doi:10.1016/j.jpowsour.2003.12.027]

Parthasarathy, A., Srinivasan, S., Appleby, J.A., Martin, C.R., 1992. Pressure dependence of the oxygen reduction reaction at the platinum microelectrode/nafion interface: electrode kinetics and mass transport. *J. Electrochem. Soc.*, **139**(10):2856-2862. [doi:10.1149/1.2068992]

Siegel, N.P., Ellis, M.W., Nelson, D.J., von Spakovsky, M.R., 2004. A 2D computational model of a PEMFC with liquid water transport. *J. Power Sources*, **128**(2):173-184. [doi:10.1016/j.jpowsour.2003.09.072]

Sivertsen, B.R., Djilali, N., 2005. CFD based modelling of proton exchange membrane fuel cells. *J. Power Sources*, **141**(1):65-78. [doi:10.1016/j.jpowsour.2004.08.054]

Springer, T.E., Zawodzinski, T.A., Gottesfeld, S., 1991. Polymer electrolyte fuel cell model. *J. Electrochem. Soc.*, **138**(8):2334-2342. [doi:10.1149/1.2085971]

Stanic, V., Hoberech, M., 2004. Mechanical of Pin-hole Formation in Membrane Electrode Assemblies for PEM Fuel Cells. Proceedings of the Fourth International Symposium on Proton Conducting Membrane Fuel Cells.

Sui, P., Djilali, N., 2005. Analysis of water transport in proton exchange membranes using a phenomenological model. *J. Fuel Cell Sci. & Tech. ASME*, **2**(1):149-155. [doi:10.1115/1.1895945]

Tang, Y., Santare, M., Karlsson, A., 2006. Stresses in proton exchange membranes due to hydro-thermal loading. *J. Fuel Cell Sci. & Tech. ASME*, **3**(2):119-124. [doi:10.1115/1.2173666]

Um, S., Wang, C.Y., 2004. 3D analysis of transport and electrochemical reactions in polymer electrolyte fuel cells. *J. Power Sources*, **125**(1):40-51. [doi:10.1016/j.jpowsour.2003.07.007]

Wang, L., Husar, A., Zhou, T., Liu, H., 2003. A parametric study of PEM fuel cell performances. *Int. J. Hydrogen Energy*, **28**(11):1263-1272. [doi:10.1016/S0360-3199(02)00284-7]